NANO LETTERS

pubs.acs.org/NanoLett
Letter

Chemical Mapping of Excitons in Halide Double Perovskites

Raisa-Ioana Biega, Yinan Chen, Marina R. Filip,* and Linn Leppert*

Cite This: *Nano Lett.* 2023, 23, 8155−8161

Read Online

ACCESS | Metrics & More | Article Recommendations | Supporting Information

ABSTRACT: Halide double perovskites comprise an emerging class of semiconductors with tremendous chemical and electronic diversity. While their band structure features can be understood from frontier-orbital models, chemical intuition for optical excitations remains incomplete. Here, we use ab initio many-body perturbation theory within the *GW* and the Bethe−Salpeter equation approach to calculate excited-state properties of a representative range of $Cs_2BB'Cl_6$ double perovskites. Our calculations reveal that double perovskites with different combinations of B and B′ cations display a broad variety of electronic band structures and dielectric properties and form excitons with binding energies ranging over several orders of magnitude. We correlate these properties with the orbital-induced anisotropy of charge-carrier effective masses and the long-range behavior of the dielectric function by comparing them with the canonical conditions of the Wannier−Mott model. Furthermore, we derive chemically intuitive rules for predicting the nature of excitons in halide double perovskites using computationally inexpensive density functional theory calculations.

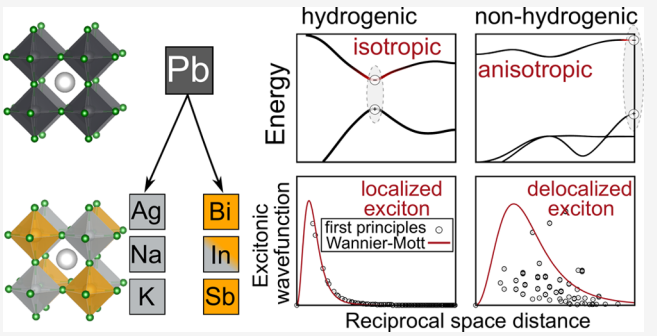

KEYWORDS: *excitons, halide perovskites, optical properties, first-principles calculations, dielectric screening*

Halide double perovskites, also known as elpasolites,[1] are a class of materials with the general formula $A_2BB'X_6$, where A is a monovalent cation such as Cs^+, balancing the charge of corner-connected BX_6 and $B'X_6$ metal halide octahedra. These stable, nontoxic, and earth-abundant semiconductors have showcased their potential in a range of applications, including photovoltaics,[2−11] X-ray detection,[12,13] radiation detection,[14−16] white light emission,[17,18] and photocatalysis.[19] This is in large part due to the tremendous chemical and structural diversity of this material class,[20−23] which can be achieved by chemical substitution at the B, B′, and X sites.[24−26]

Understanding optical excitations in halide double perovskites is crucial for designing efficient optoelectronic applications.[10,27−29] In particular, the binding energy of photoexcited electron−hole pairs (excitons) is a useful parameter to determine in studies of charge-carrier transport and recombination and is thus key for device performance and design. Experimentally, exciton binding energies of halide perovskites have been extracted from optical absorption measurements either by fitting spectra using Elliott's theory[30−32] or by measuring optical absorption spectra under high magnetic fields.[33] These methods generally assume that excitons obey the Wannier−Mott (or hydrogenic) model, which in three dimensions yields the following expression for the energies of the bound exciton states: $E_n = -\frac{\mu}{\epsilon^2}\cdot\frac{1}{n^2}$ (in atomic units), where μ is the reduced effective mass, ϵ is the dielectric constant, and n is the principal quantum number, with the binding energy defined as $E_B = -E_1$. The hydrogenic model has been used to understand the photophysics of a wide range of materials, from Pb-based halide perovskites[31,33−37] to MoS_2 and other layered materials.[38−40] Fundamentally, the hydrogenic model relies on two main assumptions, that electronic bands must be isotropic and parabolic and that the dielectric screening of the electron−hole interaction must be uniform (described by the dielectric constant).[41] The degree to which complex heterogeneous semiconductors abide by these tenets determines how accurate the hydrogenic picture is in describing excitons in a material, or (as we denote herein) how "hydrogenic" excitons are in a material.

First-principles many-body perturbation theory within the *GW* approximation[42] and the Bethe−Salpeter equation[43,44] (BSE) approach has played a particularly important role in quantitatively predicting the electronic and excited-state structure of halide perovskites. In particular, comparison of *GW*+BSE calculations with the Wannier−Mott model has demonstrated the hydrogenic nature of excitons in Pb-based halide perovskites[45,46] and in the double perovskite $Cs_2AgInCl_6$.[18,47] In contrast, we and others recently showed

Received: June 20, 2023
Revised: August 25, 2023
Published: September 1, 2023

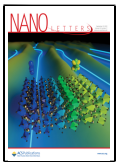

https://doi.org/10.1021/acs.nanolett.3c02285
Nano Lett. 2023, 23, 8155−8161

that the double perovskite family Cs_2AgBX_6 (B = Bi or Sb, and X = Br or Cl)[2,3,22] exhibits resonant excitons with binding energies between 170 and 450 meV, which are strongly localized, with fine structural features that differ from those computed using the hydrogenic model.[48,49] We assigned the nonhydrogenic character of excitons in these halide double perovskites to their chemical heterogeneity giving rise to an anisotropic electronic structure and dielectric screening.[49] For other halide double perovskites, optoelectronic properties and exciton binding energies were also shown to vary significantly.[50−52] The picture that emerges from these reports suggests a rich landscape of excitons in halide double perovskites and calls for systematic mapping of this landscape using first-principles calculations.

In this Letter, we use the *GW*+BSE approach to develop a holistic understanding of how the electronic structure of the alternating B- and B′-site cations influences the nature of excitons in halide double perovskites. By studying a representative set of halide double perovskites $Cs_2BB'Cl_6$, we show that exciton binding energies can be tuned by several orders of magnitude through chemical substitution at the B and B′ sites. Furthermore, we demonstrate that direct band gap halide double perovskites with isotropic, parabolic band edges and small local field effects in their dielectric screening feature hydrogenic excitons similar to their Pb-based single perovskite congeners. However, the absorption spectra of these materials depend considerably on the symmetry of the band edges and can deviate significantly from expectations prescribed by canonical models. Among the heterogeneous double perovskites we study systematically, we find that some (but not all) exhibit an exciton fine structure that is described well by the hydrogenic model. However, the extent to which excitons present as nonhydrogenic depends strongly on the electronic structure of the alternating B and B′ metals.

Recently, ref 46 showed that the fully inorganic Pb-based halide perovskites feature hydrogenic excitons. Here we use the cubic phase of $CsPbCl_3$ (termed **Pb** in the following) as a prototypical case of a direct band gap single perovskite, which we compare to seven representative cubic double perovskites $A_2BB'X_6$ with A = Cs^+ and X = Cl^- (denoted by **B**/**B′** hereafter). Our goal is to identify how the electronic structure of the B- and B′-site cations determines the hydrogenic nature of excitons in halide double perovskites. To this end, we explore double perovskites featuring metals from across the periodic table (Figure 1a): **In**/**Bi**, which is isoelectronic to **Pb**; **Ag**/**In** and **Na**/**In**, which feature a direct band gap and large band dispersion but a band edge orbital character distinctly different from that of **In**/**Bi**; and **Ag**/**Bi**, **Ag**/**Sb**, **Na**/**Bi**, and **K**/**Bi**, with an indirect band gap and low-dispersion band edges. With the exception of **In**/**Bi**, these double perovskites have all been synthesized and experimentally characterized.[2,3,18,53−59] The Na- and K-based compounds have experimentally been studied as favorable host structures for luminescent centers such as Mn^{2+} and Sb^{3+}.[57−59] However, to the best of our knowledge, we have been the first to perform state-of-the-art *GW*+BSE calculations for these materials and report their exciton binding energies.

We start by calculating the quasiparticle (QP) band structure, absorption spectra, and exciton binding energies of all eight materials using the *GW*+BSE approach as implemented in the BerkeleyGW code[60,61] (see the Supporting Information and Figures S1−S3 for further computational details and convergence studies). Figure 1b shows the exciton

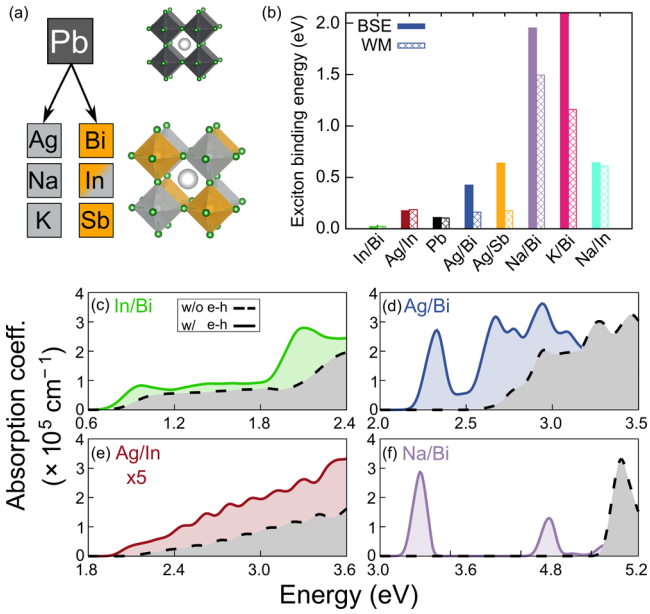

Figure 1. (a) Overview of the materials studied. In the cubic structures of single and double perovskites, X sites (Cl^-) are colored green, A sites (Cs^+) are colored white, dark gray corresponds to Pb, light gray corresponds to the B site, and orange corresponds to the B′ site. (b) Exciton binding energy computed from first principles (solid bars) and estimated on the basis of the Wannier−Mott fine structure, as described in the text (patterned bars). Materials appear in order of their QP band gap with the lowest-band gap material on the left. Linear optical absorption spectra, calculated using the independent-particle approximation (black dashed line) and the G_0W_0+BSE approach (solid colored line) for (c) **In**/**Bi**, (d) **Ag**/**Bi**, (e) **Ag**/**In**, and (f) **Na**/**Bi**.

binding energy from first-principles calculations (BSE) and estimated according to the Wannier−Mott fine structure (WM). BSE exciton binding energies (E_{BSE}) are calculated as the difference between the energy of the first excited state and the direct QP band gap. To avoid systematic errors in the calculation of the Wannier−Mott energy (see the Supporting Information for details), here, and unless otherwise noted, we quantify agreement with the Wannier−Mott model using the excitonic fine structure (excited-state energy levels) $E^{fs,WM} = \frac{4}{3}(E_{2s} - E_{1s})$, i.e., from the difference between the G_0W_0+BSE excitation energies of the 1s (E_{1s}) and 2s (E_{2s}) states, respectively (see the Supporting Information and Figure S4 for exciton fine structures and assignment of the 1s and 2s states). Table 1 reports the QP band gaps and exciton binding energies of all eight materials.

Figure 1b and Table 1 allow for several observations. First, our selected double perovskites span a wide range of QP band gaps between ∼1 and 5 eV, which are inversely proportional to their dielectric constants ε_∞ (Figure S5). The exciton binding energies of these compounds differ by several orders of magnitude with E_{BSE} ranging from 16 meV (**In**/**Bi**) to ∼2 eV (**K**/**Bi**). However, as shown in Figure S6, E_{BSE} does not scale linearly with $1/\varepsilon_\infty^2$, suggesting that the Wannier−Mott model performs poorly for a subset of double perovskites. Indeed, the first-principles exciton binding energies of **Ag**/**Bi**, **Ag**/**Sb**, **Na**/**Bi**, and **K**/**Bi** deviate by several hundred millielectronvolts from the Wannier−Mott fine structure. In contrast, and despite their seemingly similar degree of chemical heterogeneity, **Ag**/**In**, **In**/**Bi**, and **Na**/**In** feature hydrogenic excitons, similar to

https://doi.org/10.1021/acs.nanolett.3c02285
Nano Lett. 2023, 23, 8155−8161

Table 1. G_0W_0@PBE Lowest Direct Band Gaps, Static Dielectric Constants as Computed within the Random Phase Approximation, E^{BSE} Values of the First Dark and First Bright Excited States, and $E^{fs,WM}$ Values

			exciton binding energy (eV)		
			BSE		Wannier–Mott
B/B′ system	QP direct gap $E_{gap}^{G_0W_0}$ (eV)	static dielectric constant ε_∞	E_{dark}^{BSE}	E_{bright}^{BSE}	$E^{fs,WM}$
		Hydrogenic			
Pb	2.25	3.67	0.105	0.104	0.103
In/Bi	0.90	5.63	0.021	0.020	0.018
Ag/In	2.09	3.75	0.176	0.049	0.170
Na/In	5.52	2.78	0.642	0.135	0.605
		Nonhydrogenic			
Ag/Bi	2.64	4.49	0.426	0.329	0.206
Ag/Sb	3.20	4.63	0.639	0.549	0.302
Na/Bi	4.93	3.09	1.953	1.611	0.553
K/Bi	4.99	2.73	2.091	1.725	0.487

the single perovskite **Pb**.[46] We therefore separate the studied double perovskites in two groups: materials with hydrogenic (**Pb**, **Bi/In**, **Ag/In**, and **Na/In**) and materials with nonhydrogenic (**Ag/Bi**, **Ag/Sb**, **Na/Bi**, and **K/Bi**) exciton fine structures. Notably, we find that $\Delta_{WM} = E_{BSE} - E^{fs,WM}$ does not necessarily increase with exciton binding energy. In other words, the magnitude of the exciton binding energy is not sufficient to explain the observed nonhydrogenic fine structure. For example, **Na/In** features a hydrogenic 1s exciton with a very high binding energy of ∼600 meV.

Not only the exciton binding energies but also the linear optical absorption spectra of these eight materials differ significantly, as shown for representative double perovskites with hydrogenic and nonhydrogenic excitons in panels c and e and panels d and f, respectively, of Figure 1 (see also Figure S7). The absorption spectrum of **In/Bi** exhibits a distinct excitonic feature, similar to that of the isoelectronic **Pb**. In agreement with previous results,[18] we observe that **Ag/In** and **Na/In** have a weak absorption onset and do not exhibit a signature excitonic peak. The absorption coefficient is also one order of magnitude lower than that of the other materials. This is in line with the dipole-forbidden transitions between the valence and conduction band edges[62] of these materials. In contrast, all four materials with nonhydrogenic excitons feature one or several distinct excitonic peaks at the onset of absorption.

Having established these subsets of materials with hydrogenic and nonhydrogenic excitons, we continue by probing the degree to which the main assumptions of the Wannier–Mott model, isotropic, parabolic band edges and a uniform, isotropic dielectric constant, are fulfilled for these materials. We start by calculating the effective electron and hole masses at the high-symmetry point in the Brillouin zone of the lowest-energy direct transition (Table S3 and Figures S8 and S9 for density functional theory (DFT) and G_0W_0 band gaps and band structures) along the principal axes of the effective mass tensor, which can be identified as longitudinal and transverse effective masses (Table 2), similar to *fcc* semiconductors such as Si and GaAs[63] (see the Supporting Information). We show the valence and conduction band edges along those directions in panels a and b of Figure 2 for **In/Bi** and **Ag/Bi**, respectively, representative of double perovskites with hydrogenic and nonhydrogenic excitons, respectively. Around the high-symmetry point of the lowest-energy direct transition (Γ [0, 0, 0] for **In/Bi** and X [0, 1, 0]$2\pi/a$ for **Ag/Bi**), the band edges are isotropic for **In/Bi** and highly anisotropic for **Ag/Bi**, with different curvatures in the longitudinal and transverse directions.

Table 2. G_0W_0@PBE Reduced Effective Masses μ (in units of electron rest mass m_0), Anisotropy Factors λ_μ, Static Dielectric Constants (within the random phase approximation), Screening-Length Parameters, and Relative and Absolute Deviations of the Wannier–Mott Exciton Binding Energies with Respect to the First-Principles (BSE) Results

				deviation from Wannier–Mott	
B/B′ system	μ	λ_μ	screening-length parameter $l = q_{TF}/k_x$	Δ_{WM} (%)	Δ_{WM} (meV)
			Hydrogenic		
Pb	0.105	1.00	9.16	1.48	1.54
In/Bi	0.052	0.94	27.84	13.43	2.77
Ag/In	0.191	1.05	9.02	3.54	6.23
Na/In	0.345	0.96	2.71	5.73	36.74
			Nonhydrogenic		
Ag/Bi	0.241	1.29	3.82	55.82	230.83
Ag/Sb	0.250	1.23	3.57	52.66	336.38
Na/Bi	0.257	0.86	3.47	28.34	553.39
K/Bi	0.636	0.88	3.58	23.27	486.63

Further analysis reveals that the effective mass anisotropy factor $\lambda_\mu = \left(\frac{\mu_\perp}{\mu_\parallel}\right)^{1/3}$ is close to 1 for the double perovskites with hydrogenic excitons and exactly 1 for **Pb**. In Figure 2c, we show Δ_{WM} as a function of the quantity $\Lambda = |1 - \lambda_\mu|$, where $\Lambda = 0$ corresponds to a fully isotropic material (e.g., **Pb**). This analysis shows that the relative deviation from the Wannier–Mott model scales almost linearly with the degree of anisotropy. The materials with hydrogenic excitons (red squares) are mostly isotropic and feature a deviation of ≲14% from the Wannier–Mott model. In contrast, the double perovskites with nonhydrogenic excitons (blue dots) show a significantly higher degree of anisotropy and a large deviation from the Wannier–Mott model. We note that accounting for the effective mass anisotropy in the Wannier–Mott model following ref 64 decreases Δ_{WM} but does not fully account for the observed deviations (Table S4).

Next, we probe the uniformity and isotropy of the dielectric screening by computing linear absorption spectra and exciton binding energies assuming uniform dielectric screening (see the Supporting Information) and find that they change significantly only for those perovskites in which excitons do not display hydrogenic behavior (Figure S7 and Table S6). We then analyze the spatial dependence of the head (i.e., the $\mathbf{G} = \mathbf{G}' = 0$ component) of the dielectric function. Figure 3a and Figure S10 show that we can fit this spatial dependence with the model dielectric function, $\mathrm{Re}[\epsilon(q, 0)] = 1 + \left[(\varepsilon_\infty - 1)^{-1} + \alpha\left(\frac{q}{q_{TF}}\right)^2\right]^{-1}$, with α and the Thomas–Fermi wave vector, q_{TF}, as fitting parameters listed in Table S6 and ε_∞ as the RPA dielectric constant.[65]

We then compare the length scale of dielectric screening, quantified by q_{TF}, with the length scale of the excitonic wave

https://doi.org/10.1021/acs.nanolett.3c02285
Nano Lett. 2023, 23, 8155−8161

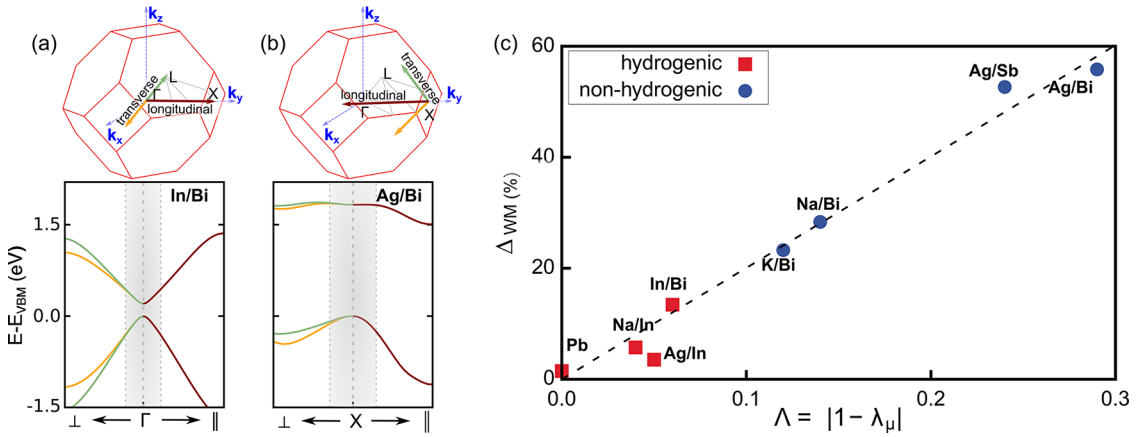

Figure 2. Graphical representation of the Brillouin zone and the DFT-PBE+SOC conduction and valence bands of (a) **In/Bi** and (b) **Ag/Bi** along the transversal (X/Γ → ⊥) and longitudinal (X/Γ → ||) directions. The shaded area corresponds to the **k**-interval used to compute the effective masses. (c) Variation of relative deviation Δ_{WM} of the Wannier−Mott fine structure with respect to the first-principles (BSE) result as a function of the effective mass anisotropy $\Lambda = |1 - \lambda_\mu|$.

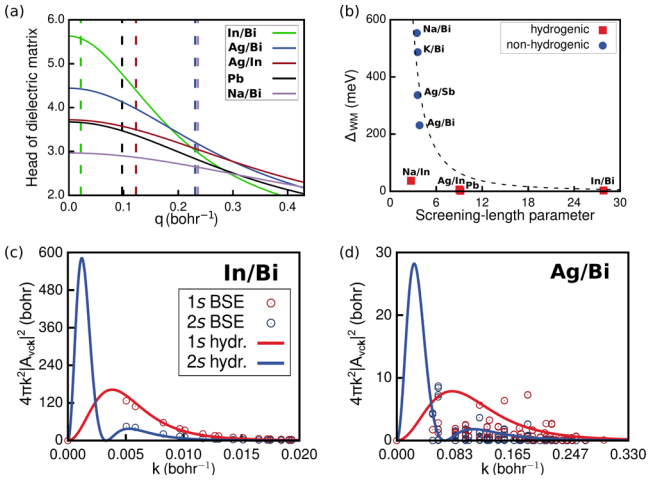

Figure 3. (a) Model dielectric function (as described in the text) in reciprocal space for **In/Bi** (green), **Ag/Bi** (blue), **Ag/In** (red), **Pb** (black), and **Na/Bi** (purple). The corresponding colored dashed line shows the exciton extent in **k**-space (k_x) as defined in the text. (b) Absolute variation of Δ_{WM} as a function of the screening-length parameter $l = \frac{q_{TF}}{k_x}$. Exciton radial probability density in reciprocal space as computed from G_0W_0+BSE (empty disks) and as predicted by the Wannier−Mott model (solid lines) for 1s (red) and 2s (blue) states for (c) **In/Bi** and (d) **Ag/Bi**.

function of the first excited state k_x in reciprocal space, by calculating the screening-length parameter $l = \frac{q_{TF}}{k_x}$ (Table 2). For this, we define k_x such that it includes 99% of the exciton probability density of the first excited state. Figure 3b shows that Δ_{WM} decreases as $1/l^2$. Perovskites with hydrogenic excitons feature large screening-length parameters ($l \geq 11$), corresponding to excitons highly localized in reciprocal space for which the dielectric screening can be assumed to be uniform and constant. An outlier is **Na/In** with $l = 2.71$, closer to the values of the materials with nonhydrogenic excitons. We attribute this to the slow variation of the dielectric function in reciprocal space in this large-band gap compound (Figure S10). In contrast, for the subset of materials with non-hydrogenic excitons, the variation of the dielectric constant is significant on the length scale of their excitons, strongly delocalized in reciprocal space. Deviations from the Wannier−Mott model in these materials are also apparent by comparing the excitonic wave functions computed with G_0W_0+BSE with the radial probability density of hydrogenic 1s and 2s excitonic wave functions, shown in panels c and d of Figure 3 for **In/Bi** and **Ag/Bi**, respectively (see Figure S11 for the other materials).

Finally, we return to our goal of mapping the character of excitons in halide double perovskites to the band edge electronic structure obtained from computationally inexpensive DFT calculations (instead of a full solution of the BSE). We note that the effective mass anisotropy can be approximated by using DFT effective masses (see Table S3). Chemical intuition for the reciprocal space location, parity, and dispersion of the VBM and CBM can be obtained on the basis of the metal-orbital character of the band edges of halide perovskites, as shown in ref 66 using linear combinations of atomic orbitals and symmetry arguments. Table 3 shows the calculated B-site orbital character and the high-symmetry **k**-point of the VBM and CBM of all eight perovskites, in agreement with previous predictions,[66] and lists the B-site orbital character at the lowest direct transition from which excitons are derived. We observe that in all materials with nonhydrogenic excitons, the B-site orbital contributions to the band edges lead to an indirect band gap. The lowest direct transition in these materials occurs at the Brillouin zone boundaries (X in **Ag/Bi** and **Ag/Sb** and L in **K/Bi** and **Na/Bi**). Furthermore, in all of those materials, the conduction band edge at the lowest direct transition is relatively flat along the transverse directions, which is a consequence of small B- and B′-site orbital overlap. In **Ag/Bi** and **Ag/Sb**, there is no Ag s character at the X points due to orbital symmetry. In **Na/Bi** and **K/Bi**, Na s and K s contribute to the conduction band edge at L but their overlap with the neighboring Bi p orbitals is small, leading to high effective masses in the transverse direction.

In materials with hydrogenic excitons, there is a symmetry match of the B- and B′-site orbitals leading to a direct band gap at Γ with isotropic effective masses. Note that a direct gap can also arise in a double perovskite in which only one or none of the metal sites contributes to the band edges.[66] In **Na/In**, the valence band edge is rather flat, because it does not feature metal-site orbital contributions. However, the conduction band

https://doi.org/10.1021/acs.nanolett.3c02285
Nano Lett. 2023, 23, 8155−8161

Table 3. Metal-Orbital Character of the Band Edges, Nature of the Band Gap, Effective Mass Anisotropy, and Nature of the Exciton for the Analyzed Materials and Vacancy-Ordered Perovskites Cs_2TeBr_6, Cs_2TiBr_6, and Cs_2SnBr_6[a]

	band gap			lowest direct trans.			anisotropy		
system	valence	conduction	k-point	valence	conduction	k-point	predicted	calculated	exciton
Ag/Bi	Ag $4d_{z^2}$ Bi 6s	Ag 5s Bi 6p	indirect X → L	Ag $4d_{z^2}$ Bi 6s	null Bi 6p	X	high Λ	high Λ	nonhydr.
Ag/Sb	Ag $4d_{z2}$ Sb 5s	Ag 5s Sb 5p	indirect X → L	Ag $4d_{z^2}$ Sb 5s	null Sb 5p	X	high Λ	high Λ	nonhydr.
K/Bi	null Bi 6s	K 4s Bi 6p	indirect L → Γ direct Γ	null Bi 6s	K 4s Bi 6p	L	high Λ	high Λ	nonhydr.
Na/Bi	null Bi 6s	Bi 6p Na 3s	indirect X → Γ	null Bi 6s	Na 3s Bi 6p	L	high Λ	high Λ	nonhydr.
Ag/In	Ag $4d_{z^2/x^2-y^2}$ null	Ag 5s In 5s	direct Γ	Ag $4d_{z^2/x^2-y^2}$ null	Ag 5s In 5s	Γ	low Λ	low Λ	hydr.
Na/In	null null	Na 3s In 5s	direct Γ	null null	Na 3s In 5s	Γ	low Λ	low Λ	hydr.
In/Bi	In 5s Bi 6s	In 5p Bi 6p	direct Γ	In 5s Bi 6s	In 5p Bi 6p	Γ	low Λ	low Λ	hydr.
Pb	Pb 6s	Pb 6p	direct R	Pb 6s	Pb 6p	R	no Λ	no Λ	hydr.
Cs_2TeBr_6	Te 6s	Te 6p	indirect X → L	Te 6s	Te 6p	L	high Λ	high Λ	nonhydr.
Cs_2TiBr_6	null	Ti $3d_{xy}$	indirect Γ → X	null	Ti $3d_{xy}$	Γ	high Λ	high Λ	nonhydr.
Cs_2SnBr_6	null	Sn 5s	direct Γ	null	Sn 5s	Γ	low Λ	low Λ	hydr.

[a]Contributions from halogen atoms have been omitted for the sake of clarity.

minimum, with contributions from Na s and In s, is at Γ, disperse, and isotropic.

Our predictions can also be extended to double perovskites with only one B site, such as the vacancy-ordered perovskites with a chemical formula of Cs_2BX_6. *GW*+BSE calculations by Cucco et al. for Cs_2TeBr_6 and Kavanagh et al. for Cs_2TiX_6 (X = I, Br, and Cl) indicate excitons highly localized in real space and ill-described by the Wannier−Mott model for these materials.[67,68] Cs_2SnX_6, on the contrary, features hydrogenic excitons, as reported in refs 67 and 68. Using Cs_2TeBr_6, Cs_2TiBr_6, and Cs_2SnBr_6 as examples, we calculated the orbital character of the band edges and effective mass anisotropy using DFT (Table S7). The band structure of Cs_2TeBr_6 is reminiscent of that of **Ag/Bi** and **Ag/Sb** with Te 6s and 6p contributions, leading to an indirect band gap. The lowest direct transition is at L, where the conduction band is derived from Te p orbitals alone and therefore anisotropic. Cs_2TiBr_6 is another indirect gap semiconductor. Its relatively flat and highly anisotropic conduction band is derived from localized Ti d states and features weak Ti d−X p mixing. Cs_2SnBr_6, on the contrary, is comparable to **Na/In** with a direct band gap at Γ and an isotropic conduction band derived from Sn s orbitals (Table 3). In summary, for the systems analyzed here, an effective mass anisotropy factor of >0.1 appears to be sufficient to predict a nonhydrogenic excitonic fine structure. However, as shown in Tables S4 and S5, the effective mass anisotropy is only one contributing factor, alongside the non-uniformity of the dielectric function, in particular in materials with larger dielectric constants.

In conclusion, we performed a detailed first-principles study of the optoelectronic properties of a set of representative $Cs_2BB'Cl_6$ double perovskites and compared them with those of the single perovskite $CsPbCl_3$ with its known hydrogenic exciton series. Chemical substitution at the B and B′ metal sites allows for the realization of a wide variety of electronic structure properties with significant orbital-dependent effects on the anisotropy of charge-carrier effective masses and dielectric screening. Our calculations show that the chemical heterogeneity inherently present in double perovskites leads to nonhydrogenic excitons only for B- and B′-site combinations that result in indirect band gaps and large effective mass anisotropies at the band edges. In these double perovskites, excitons are strongly delocalized in reciprocal space and thus experience the full spatial variation of dielectric screening. We show that our understanding of excitons in halide double perovskites can be extended to vacancy-ordered perovskites with a single B site. The nature of excitons in double perovskites can thus be predicted on the basis of computationally efficient DFT calculations. With these insights, our state-of-the-art *GW*+BSE calculations can provide a starting point for the development of tight-binding models for excitons, aid in the interpretation of experiments, and inspire further study of excited-state properties of this complex quarternary family of materials.

■ ASSOCIATED CONTENT

Supporting Information

The Supporting Information is available free of charge at https://pubs.acs.org/doi/10.1021/acs.nanolett.3c02285.

Methodological and computational details (including convergence plots), DFT and QP electronic band structures, absorption spectra, exciton diagrams, radial probability density, and variation of the dielectric constant in reciprocal space (PDF)

Structure files used in calculations (ZIP)

■ AUTHOR INFORMATION

Corresponding Authors

Marina R. Filip − *Department of Physics, University of Oxford, Oxford OX1 3PU, United Kingdom;* orcid.org/0000-0003-2925-172X; Email: marina.filip@physics.ox.ac.uk

Linn Leppert − *MESA+ Institute for Nanotechnology, University of Twente, 7500 AE Enschede, The Netherlands;*

https://doi.org/10.1021/acs.nanolett.3c02285
Nano Lett. 2023, 23, 8155−8161

orcid.org/0000-0002-4361-4382; Email: l.leppert@utwente.nl

Authors

Raisa-Ioana Biega − *MESA+ Institute for Nanotechnology, University of Twente, 7500 AE Enschede, The Netherlands;* orcid.org/0009-0001-2042-1895

Yinan Chen − *Department of Physics, University of Oxford, Oxford OX1 3PU, United Kingdom;* orcid.org/0000-0002-0173-6197

Complete contact information is available at: https://pubs.acs.org/10.1021/acs.nanolett.3c02285

Notes

The authors declare no competing financial interest.

■ ACKNOWLEDGMENTS

The authors acknowledge computing resources provided by the Dutch national supercomputing center Snellius supported by the SURF Cooperative and PRACE for awarding access to the Marconi100 supercomputer at CINECA, Italy. This work was partially supported by the Dutch Research Council (NWO) under Grant OCENW.M20.337. M.R.F. and Y.C. gratefully acknowledge access to additional computational resources used for some of these calculations, provided by the Extreme Science and Engineering Discovery Environment (now ACCESS) to supercomputer Stampede2 at the Texas Advanced Computing Center (TACC) through Allocation TG-DMR190070. M.R.F. acknowledges support from the UK Engineering and Physical Sciences Research Council (EPSRC) via Grant EP/V010840/1.

■ REFERENCES

(1) Cross, C. W.; Hillebrand, W. F. On minerals of the cryolite group recently found in Colorado. *Am. J. Sci.* **1883**, *s3*−*26*, 271−294.
(2) McClure, E. T.; Ball, M. R.; Windl, W.; Woodward, P. M. Cs_2AgBiX_6 (X = Br, Cl) — New visible light absorbing, lead-free halide perovskite semiconductors. *Chem. Mater.* **2016**, *28*, 1348−1354.
(3) Slavney, A. H.; Hu, T.; Lindenberg, A. M.; Karunadasa, H. I. A Bismuth-Halide Double Perovskite with Long Carrier Recombination Lifetime for Photovoltaic Applications. *J. Am. Chem. Soc.* **2016**, *138*, 2138−2141.
(4) Greul, E.; Petrus, M. L.; Binek, A.; Docampo, P.; Bein, T. Highly stable, phase pure $Cs_2AgBiBr_6$ double perovskite thin films for optoelectronic applications. *J. Mater. Chem. A* **2017**, *5*, 19972−19981.
(5) Zhao, X.-G.; Yang, J.-H.; Fu, Y.; Yang, D.; Xu, Q.; Yu, L.; Wei, S.-H.; Zhang, L. Design of Lead-Free Inorganic Halide Perovskites for Solar Cells via Cation-Transmutation. *J. Am. Chem. Soc.* **2017**, *139*, 2630−2638.
(6) Volonakis, G.; Haghighirad, A. A.; Milot, R. L.; Sio, W. H.; Filip, M. R.; Wenger, B.; Johnston, M. B.; Herz, L. M.; Snaith, H. J.; Giustino, F. $Cs_2InAgCl_6$: A New Lead-free Halide Double Perovskite with Direct Band Gap. *J. Phys. Chem. Lett.* **2017**, *8*, 772−778.
(7) Debbichi, L.; Lee, S.; Cho, H.; Rappe, A. M.; Hong, K.-H.; Jang, M. S.; Kim, H. Mixed Valence Perovskite $Cs_2Au_2I_6$: A Potential Material for Thin-Film Pb-Free Photovoltaic Cells with Ultrahigh Efficiency. *Adv. Mater.* **2018**, *30*, 1707001.
(8) Fakharuddin, A.; Shabbir, U.; Qiu, W.; Iqbal, T.; Sultan, M.; Heremans, P.; Schmidt-Mende, L. Inorganic and Layered Perovskites for Optoelectronic Devices. *Adv. Mater.* **2019**, *31*, 1807095.
(9) Yang, X.; Chen, Y.; Liu, P.; Xiang, H.; Wang, W.; Ran, R.; Zhou, W.; Shao, Z. Simultaneous Power Conversion Efficiency and Stability Enhancement of $Cs_2AgBiBr_6$ Lead-Free Inorganic Perovskite Solar Cell through Adopting a Multifunctional Dye Interlayer. *Adv. Funct. Mater.* **2020**, *30*, 2001557.
(10) Longo, G.; Mahesh, S.; Buizza, L. R. V.; Wright, A. D.; Ramadan, A. J.; Abdi-Jalebi, M.; Nayak, P. K.; Herz, L. M.; Snaith, H. J. Understanding the Performance-Limiting Factors of $Cs_2AgBiBr_6$ Double-Perovskite Solar Cells. *ACS Energy Lett.* **2020**, *5*, 2200−2207.
(11) Sirtl, M. T.; Hooijer, R.; Armer, M.; Ebadi, F. G.; Mohammadi, M.; Maheu, C.; Weis, A.; van Gorkom, B. T.; Häringer, S.; Janssen, R. A. J.; Mayer, T.; Dyakonov, V.; Tress, W.; Bein, T. 2D/3D Hybrid $Cs_2AgBiBr_6$ Double Perovskite Solar Cells: Improved Energy Level Alignment for Higher Contact-Selectivity and Large Open Circuit Voltage. *Adv. Energy Mater.* **2022**, *12*, 2103215.
(12) Pan, W.; et al. $Cs_2AgBiBr_6$ single-crystal X-ray detectors with a low detection limit. *Nat. Photonics* **2017**, *11*, 726−732.
(13) Steele, J. A.; et al. Photophysical Pathways in Highly Sensitive $Cs_2AgBiBr_6$ Double-Perovskite Single-Crystal X-Ray Detectors. *Adv. Mater.* **2018**, *30*, 1804450.
(14) Brittain, H. G.; Meyer, G. Cryogenic luminescence studies of Eu^{3+} in $LiEuCl_4$. *J. Solid State Chem.* **1985**, *59*, 183−189.
(15) Pawlik, T.; Spaeth, J.-M. Investigation of Radiation-Induced Defects in Cs_2NaYF_6. *Phys. Status Solidi B* **1997**, *203*, 43−52.
(16) Biswas, K.; Du, M. H. Energy transport and scintillation of cerium-doped elpasolite Cs_2LiYCl_6: Hybrid density functional calculations. *Phys. Rev. B* **2012**, *86*, 014102.
(17) Yang, B.; Mao, X.; Hong, F.; Meng, W.; Tang, Y.; Xia, X.; Yang, S.; Deng, W.; Han, K. Lead-Free Direct Band Gap Double-Perovskite Nanocrystals with Bright Dual-Color Emission. *J. Am. Chem. Soc.* **2018**, *140*, 17001−17006.
(18) Luo, J.; et al. Efficient and stable emission of warm-white light from lead-free halide double perovskites. *Nature* **2018**, *563*, 541−545.
(19) Muscarella, L. A.; Hutter, E. M. Halide Double-Perovskite Semiconductors beyond Photovoltaics. *ACS Energy Lett.* **2022**, *7*, 2128−2135.
(20) Brandt, R. E.; Stevanović, V.; Ginley, D. S.; Buonassisi, T. Identifying defect-tolerant semiconductors with high minority carrier lifetimes: Beyond hybrid lead halide perovskites. *MRS Commun.* **2015**, *5*, 265−275.
(21) Faber, F. A.; Lindmaa, A.; Von Lilienfeld, O. A.; Armiento, R. Machine Learning Energies of 2 Million Elpasolite (ABC_2D_6) Crystals. *Phys. Rev. Lett.* **2016**, *117*, 135502.
(22) Volonakis, G.; Filip, M. R.; Haghighirad, A. A.; Sakai, N.; Wenger, B.; Snaith, H. J.; Giustino, F. Lead-Free Halide Double Perovskites via Heterovalent Substitution of Noble Metals. *J. Phys. Chem. Lett.* **2016**, *7*, 1254−1259.
(23) Filip, M. R.; Giustino, F. The geometric blueprint of perovskites. *Proc. Nat. Acad. Sci.* **2018**, *115*, 5397−5402.
(24) Deng, Z.; Wei, F.; Sun, S.; Kieslich, G.; Cheetham, A. K.; Bristowe, P. D. Exploring the properties of lead-free hybrid double perovskites using a combined computational-experimental approach. *J. Mater. Chem. A* **2016**, *4*, 12025−12029.
(25) Jain, A.; Voznyy, O.; Sargent, E. H. High-Throughput Screening of Lead-Free Perovskite-like Materials for Optoelectronic Applications. *J. Phys. Chem. C* **2017**, *121*, 7183.
(26) Wolf, N. R.; Connor, B. A.; Slavney, A. H.; Karunadasa, H. I. Doubling the Stakes: The Promise of Halide Double Perovskites. *Ang. Chem. Int. Ed.* **2021**, *60*, 16264−16278.
(27) Schade, L.; Wright, A. D.; Johnson, R. D.; Dollmann, M.; Wenger, B.; Nayak, P. K.; Prabhakaran, D.; Herz, L. M.; Nicholas, R.; Snaith, H. J.; Radaelli, P. G. Structural and Optical Properties of $Cs_2AgBiBr_6$ Double Perovskite. *ACS Energy Lett.* **2019**, *4*, 299−305.
(28) Roknuzzaman, M.; Zhang, C.; Ostrikov, K. K.; Du, A.; Wang, H.; Wang, L.; Tesfamichael, T. Electronic and optical properties of lead-free hybrid double perovskites for photovoltaic and optoelectronic applications. *Sci. Rep.* **2019**, *9*, 718.
(29) Dey, A.; Richter, A. F.; Debnath, T.; Huang, H.; Polavarapu, L.; Feldmann, J. Transfer of Direct to Indirect Bound Excitons by Electron Intervalley Scattering in $Cs_2AgBiBr_6$ Double Perovskite Nanocrystals. *ACS Nano* **2020**, *14*, 5855−5861.
(30) Elliott, R. J. Intensity of optical absorption by excitons. *Phys. Rev.* **1957**, *108*, 1384−1389.

(31) Davies, C. L.; Filip, M. R.; Patel, J. B.; Crothers, T. W.; Verdi, C.; Wright, A. D.; Milot, R. L.; Giustino, F.; Johnston, M. B.; Herz, L. M. Bimolecular recombination in methylammonium lead triiodide perovskite is an inverse absorption process. *Nat. Commun.* **2018**, *9*, 293.
(32) Wright, A. D.; Buizza, L. R.; Savill, K. J.; Longo, G.; Snaith, H. J.; Johnston, M. B.; Herz, L. M. Ultrafast Excited-State Localization in $Cs_2AgBiBr_6$Double Perovskite. *J. Phys. Chem. Lett.* **2021**, *12*, 3352−3360.
(33) Miyata, A.; Mitioglu, A.; Plochocka, P.; Portugall, O.; Wang, J. T.-W.; Stranks, S. D.; Snaith, H. J.; Nicholas, R. J. Direct measurement of the exciton binding energy and effective masses for charge carriers in organic−inorganic tri-halide perovskites. *Nat. Phys.* **2015**, *11*, 582−587.
(34) Hirasawa, M.; Ishihara, T.; Goto, T.; Uchida, K.; Miura, N. Magnetoabsorption of the lowest exciton in perovskite-type compound $(CH_3NH_3)PbI_3$. *Physica B Condens. Matter* **1994**, *201*, 427−430.
(35) Tanaka, K.; Takahashi, T.; Ban, T.; Kondo, T.; Uchida, K.; Miura, N. Comparative study on the excitons in lead-halide-based perovskite-type crystals $CH_3NH_3PbBr_3$ $CH_3NH_3PbI_3$. *Solid State Commun.* **2003**, *127*, 619−623.
(36) Galkowski, K.; Mitioglu, A.; Miyata, A.; Plochocka, P.; Portugall, O.; Eperon, G. E.; Wang, J. T.-W.; Stergiopoulos, T.; Stranks, S. D.; Snaith, H.; Nicholas, R. J. Determination of the exciton binding energy and effective masses for methylammonium and formamidinium lead tri-halide perovskite semiconductors. *Energy Environ. Sci.* **2016**, *9*, 962−970.
(37) Wang, S.; Dyksik, M.; Lampe, C.; Gramlich, M.; Maude, D. K.; Baranowski, M.; Urban, A. S.; Plochocka, P.; Surrente, A. Thickness-Dependent Dark-Bright Exciton Splitting and Phonon Bottleneck in $CsPbBr_3$-Based Nanoplatelets Revealed via Magneto-Optical Spectroscopy. *Nano Lett.* **2022**, *22*, 7011−7019.
(38) Chernikov, A.; Berkelbach, T. C.; Hill, H. M.; Rigosi, A.; Li, Y.; Aslan, B.; Reichman, D. R.; Hybertsen, M. S.; Heinz, T. F. Exciton Binding Energy and Nonhydrogenic Rydberg Series in Monolayer WS_2. *Phys. Rev. Lett.* **2014**, *113*, 076802.
(39) Selig, M.; Berghäuser, G.; Raja, A.; Nagler, P.; Schüller, C.; Heinz, T. F.; Korn, T.; Chernikov, A.; Malic, E.; Knorr, A. Excitonic linewidth and coherence lifetime in monolayer transition metal dichalcogenides. *Nat. Commun.* **2016**, *7*, 13279.
(40) Raja, A.; et al. Coulomb engineering of the bandgap and excitons in two-dimensional materials. *Nat. Commun.* **2017**, *8*, 15251.
(41) Wannier, G. H. The Structure of Electronic Excitation Levels in Insulating Crystals. *Phys. Rev.* **1937**, *52*, 191−197.
(42) Fetter, A.; Walecka, J. *Quantum Theory of Many-Particle Systems*; MacGraw-Hill: New York, 1971.
(43) Rohlfing, M.; Louie, S. G. Electron-hole excitations in semiconductors and insulators. *Phys. Rev. Lett.* **1998**, *81*, 2312−2315.
(44) Rohlfing, M.; Louie, S. G. Electron-hole excitations and optical spectra from first principles. *Phys. Rev. B* **2000**, *62*, 4927.
(45) Bokdam, M.; Sander, T.; Stroppa, A.; Picozzi, S.; Sarma, D. D.; Franchini, C.; Kresse, G. Role of Polar Phonons in the Photo Excited State of Metal Halide Perovskites. *Sci. Rep.* **2016**, *6*, 28618.
(46) Filip, M. R.; Haber, J. B.; Neaton, J. B. Phonon Screening of Excitons in Semiconductors: Halide Perovskites and beyond. *Phys. Rev. Lett.* **2021**, *127*, 067401.
(47) Jain, M.; Bhumla, P.; Kumar, M.; Bhattacharya, S. Lead-Free Alloyed Double Perovskites: An Emerging Class of Materials for Optoelectronic Applications. *J. Phys. Chem. C* **2022**, *126*, 6753−6760.
(48) Palummo, M.; Berrios, E.; Varsano, D.; Giorgi, G. Optical Properties of Lead-Free Double Perovskites by Ab Initio Excited-State Methods. *ACS Energy Lett.* **2020**, *5*, 457−463.
(49) Biega, R. I.; Filip, M. R.; Leppert, L.; Neaton, J. B. Chemically Localized Resonant Excitons in Silver-Pnictogen Halide Double Perovskites. *J. Phys. Chem. Lett.* **2021**, *12*, 2057−2063.
(50) Luo, M.; Zhao, Y.; Yang, A.; Chen, Q.; Zhang, X.; Luo, J. First-principles study on the electronic structures and optical properties of Cs_2XInCl_6 (X= Ag, Na). *Solid State Commun.* **2022**, *352*, 114812.
(51) Yu, C.-J.; Ri, I.-C.; Ri, H.-M.; Jang, J.-H.; Kim, Y.-S.; Jong, U.-G. First-principles study on structural, electronic and optical properties of halide double perovskite Cs_2AgBX_6 (B = In, Sb; X = F, Cl, Br, I). *RSC Adv.* **2023**, *13*, 16012−16022.
(52) Adhikari, S.; Johari, P. Theoretical insights into monovalent-metal-cation transmutation effects on lead-free halide double perovskites for optoelectronic applications. *Phys. Rev. Materials* **2023**, *7*, 075401.
(53) Tran, T. T.; Panella, J. R.; Chamorro, J. R.; Morey, J. R.; McQueen, T. M. Designing indirect-direct bandgap transitions in double perovskites. *Mater. Horiz.* **2017**, *4*, 688−693.
(54) Steele, J. A.; et al. Perovskite-Based Devices: Photophysical Pathways in Highly Sensitive $Cs_2AgBiBr_6$ Double-Perovskite Single-Crystal X-Ray Detectors. *Adv. Mater.* **2018**, *30*, 1870353.
(55) Bartesaghi, D.; Slavney, A. H.; Gélvez-Rueda, M. C.; Connor, B. A.; Grozema, F. C.; Karunadasa, H. I.; Savenije, T. J. Charge Carrier Dynamics in $Cs_2AgBiBr_6$ Double Perovskite. *J. Phys. Chem. C* **2018**, *122*, 4809−4816.
(56) Dahl, J. C.; Osowiecki, W. T.; Cai, Y.; Swabeck, J. K.; Bekenstein, Y.; Asta, M.; Chan, E. M.; Alivisatos, A. P. Probing the Stability and Band Gaps of $Cs_2AgInCl_6$ and $Cs_2AgSbCl_6$ Lead-Free Double Perovskite Nanocrystals. *Chem. Mater.* **2019**, *31*, 3134−3143.
(57) Majher, J. D.; Gray, M. B.; Strom, T. A.; Woodward, P. M. $Cs_2NaBiCl_6$:Mn^{2+} - A New Orange-Red Halide Double Perovskite Phosphor. *Chem. Mater.* **2019**, *31*, 1738−1744.
(58) Noculak, A.; Morad, V.; McCall, K. M.; Yakunin, S.; Shynkarenko, Y.; Worle, M.; Kovalenko, M. V. Bright Blue and Green Luminescence of Sb(III) in Double Perovskite Cs_2MInCl_6(M = Na, K) Matrices. *Chem. Mater.* **2020**, *32*, 5118−5124.
(59) Gray, M. B.; Hariyani, S.; Strom, T. A.; Majher, J. D.; Brgoch, J.; Woodward, P. M. High-efficiency blue photoluminescence in the $Cs_2NaInCl_6$:Sb^{3+} double perovskite phosphor. *J. Mater. Chem. C* **2020**, *8*, 6797−6803.
(60) Deslippe, J.; Samsonidze, G.; Strubbe, D. A.; Jain, M.; Cohen, M. L.; Louie, S. G. BerkeleyGW: A massively parallel computer package for the calculation of the quasiparticle and optical properties of materials and nanostructures. *Comput. Phys. Commun.* **2012**, *183*, 1269−1289.
(61) Barker, B. A.; Deslippe, J.; Lischner, J.; Jain, M.; Yazyev, O. V.; Strubbe, D. A.; Louie, S. G. Spinor GW/Bethe-Salpeter calculations in BerkeleyGW: Implementation, symmetries, benchmarking, and performance. *Phys. Rev. B* **2022**, *106*, 115127.
(62) Meng, W.; Wang, X.; Xiao, Z.; Wang, J.; Mitzi, D. B.; Yan, Y. Parity-Forbidden Transitions and Their Impacts on the Optical Absorption Properties of Lead-Free Metal Halide Perovskites and Double Perovskites. *J. Phys. Chem. Lett.* **2017**, *8*, 2999−3007.
(63) Yu, P. Y.; Cardona, M. *Fundamentals of Semiconductors*, 4th ed.; Springer-Verlag: Berlin, 2010; p 171.
(64) Schindlmayr, A. Excitons with anisotropic effective mass. *Euro. J. Phys.* **1997**, *18*, 374−376.
(65) Cappellini, G.; Del Sole, R.; Reining, L.; Bechstedt, F. Model dielectric function for semiconductors. *Phys. Rev. B* **1993**, *47*, 9892−9895.
(66) Slavney, A. H.; Connor, B. A.; Leppert, L.; Karunadasa, H. I. A pencil-and-paper method for elucidating halide double perovskite band structures. *Chem. Sci.* **2019**, *10*, 11041.
(67) Kavanagh, S. R.; Savory, C. N.; Liga, S. M.; Konstantatos, G.; Walsh, A.; Scanlon, D. O. Frenkel Excitons in Vacancy-Ordered Titanium Halide Perovskites (Cs_2TiX_6). *J. Phys. Chem. Lett.* **2022**, *13*, 10965−10975.
(68) Cucco, B.; Katan, C.; Even, J.; Kepenekian, M.; Volonakis, G. Fine Structure of Excitons in Vacancy-Ordered Halide Double Perovskites. *ACS Mater. Lett.* **2023**, *5*, 52−59.

https://doi.org/10.1021/acs.nanolett.3c02285
Nano Lett. 2023, 23, 8155−8161